Intra-hour energy potential forecasting in a central solar power plant receiver combining Meteosat images and atmospheric extinction

J. Alonso-Montesinos[a,b,*], R. Monterreal[c], J. Fernández-Reche[c], J. Ballestrín[c], E. Carra[c], J. Polo[d], J. Barbero[a], F. J. Batlles[a,b], G. López[e], R. Enrique[c], M. Martínez-Durbán[f], A. Marzo[g]

[a] *Department of Chemistry and Physics, University of Almería, 04120 Almería, Spain.*
[b] *CIESOL, Joint Centre of the University of Almería-CIEMAT, 04120 Almería, Spain.*
[c] *Concentrating Solar System Unit (Plataforma Solar de Almería, CIEMAT), 04200 Almería, Spain.*
[d] *Photovoltaic Solar Energy Unity (Renewable Energy Division-CIEMAT, 28040 Madrid, Spain*
[e] *Department of Electrical and Thermal Engineering, Design and Projects, University of Huelva, 21004, Huelva, Spain.*
[f] *Department of Informatics, University of Almería, 04120 Almería, Spain*
[g] *CDEA, University of Antofagasta, 02800 Antofagasta, Chile*

Abstract

In the search for techniques that control the final energy reaching the receivers of central solar power plants, this work presents a novel combination of several methodologies for establishing a complex and valuable system within the user operating system.

*Corresponding author: Telephone: +34 950 214430
Email address: joaquin.alonso@ual.es (J. Alonso-Montesinos)

To establish the final energy level in the central receiver, the direct normal irradiance (DNI) was predicted at ground level using METEOSAT images combined with a novel system involving two digital cameras that determine atmospheric *Extinction* in the lower atmospheric layer. The predicted values were used as inputs for a solar plant model (Fiat-Lux) to trace the path of the sunlight according to the mirror features. The flux simulations presented a normalized root-mean square error (nRMSE) below 6% and correlation coefficients (R) above 0.94 when compared to real and predicted values. Therefore, it would be possible to quantify the losses produced in the path between the heliostats and the central receiver by integrating different technologies.
Keywords: DNI forecasting, Flux prediction, CSTP plant, MSG imagery, Extinction

1. Introduction

The construction of Central Solar-Tower Power (CSTP) plants has increased significantly around the world over the last few decades. Their function is to produce electricity by concentrating sunlight from heliostats onto a receiver placed at the top of a central tower. Solar-tower power plants are of interest to the CSP industry due to their greater efficiency resulting from the higher working temperatures and the possibility of operating with high

capacity thermal storage systems. Many recent solar power system projects and deployments have included at least one solar-tower plant in their plans. The capability of these plants allows us to include thermal storage systems; this is because of the large solar field comprising thousands of heliostats that concentrate the incoming direct solar irradiance onto the receiver at the top of the tower. Normally, molten salts are used as the heat transfer fluid for the thermal storage. Different studies have assessed the possibility to construct CSTP plants in the appropriate climate places, such as Algeria and China [1, 2]. Moreover, the importance of this technology has caused the development of tools to determine the optimal performance of this kind of solar plants [3].

Cloud transients have a negative effect on the plant's final production and on the peak of the transfer fluid's heat flux [4], making it necessary to adapt the plant's management to the variable climatic conditions. Considering this factor, one has to evaluate the importance of the features that affect the variability, looking for new strategies to assist the plant's operators. Variations in cloud position and form are presented in solar system literature. Predicting solar radiation when it appears in smaller timesteps is unattainable given the variability of clouds [5]; in particular, transients of clouds provoke

a decrease in solar irradiance, which come in the form of ramps, and pose a challenge to energy-load balancing in a spatially distributed network; for example, on solar farms.

The short-term evolution of the cloud field may simply be approximated translationally to first order, but care must be taken about how the advection is handled and where the impacts are assigned [6]. In addition, not all the incoming radiation hitting the mirror surfaces reach the receiver. Most CTSP plants are located in areas with low or medium probability of cloud occurrence but with a high probability that episodes of high aerosol or dust intrusion concentrations will occur [7, 8]. In a CTSP plant, the solar energy reflected by the concentrating mirrors is attenuated by the atmospheric constituents as it travels to the receiver tower [9, 10, 11]. There are geographical points where the presence of dust episodes is more frequent than in other places, like the Iberian Peninsula which has suffered several dust episodes from Sahara desert [12, 13].

Some tools, like System Advisor Model (SAM) try to replicate the final production of concentration solar plants which is served like a general idea about energy generation [14, 15]. Unfortunately, this atmospheric mirror-to-tower attenuation is given a minor importance amongst the ray-tracing

and plant optimization tools, most of which codes are limited to only two different turbidity conditions (DELSOL [16], MIRVAL [17], among others). This problem, which limits the size and geometry of the solar-tower plant field, is considered by ray-tracing and plant optimization tools for standard atmospheric conditions. That is why it is necessary to include both factors, in order to properly evaluate and predict the direct radiation values in the tower receiver [18, 19].

Appropriate control of the heat flux distribution and thermal loads on the solar central receiver is essential in order to achieve an efficient and safe operation of the solar-tower systems [20, 21, 22]. One important conclusion from these articles is that a control strategy (based on forecasting) contributes to a continuous and safe performance of the solar central receiver when subject to transient flux distribution.

Some researchers have determined that the use of satellite images is a good option in order to study the particular vertical atmospheric column present at a specific location, which includes the influence of dust on the final daily DNI forecasting [23]. Other authors have combined satellite observations from the MODIS and CALIPSO satellites with AERONET measurements, the radiative transfer model and the chemical transport model [24]. In this work, the

authors show daily DNI predictions attenuated to a degree, reaching values of 80-90% during extreme dust episodes. In this work, the authors show that the daily DNI predictions were attenuated to a degree, reaching values of 80-90% during extreme dust episodes. Based on DNI, temperature, relative humidity and atmospheric pressure, a model of atmospheric transmittance was developed for CTSP plants [25]. The model was validated in three different places of Spain and Morocco, presenting a root mean square error between 5 and 8%. Moreover, the atmospheric extinction was calculated by a simulation tool at the Plataforma Solar de Almería (PSA), presenting losses between 1.6 and 7% [26]. However, the solar extinction has been determined physically by a sophisticated system using two digital cameras [27] at the PSA, where after nearly one year of measurements, the authors determined that, under haze episodes, the extinction can reach values near to 20%.

When studying these publications, there are two important issues to deal with: firstly, the spatial vision and the temporal resolution that limit the satellite information (there are many situations in which the satellite cannot provide optimal information because of the atmospheric composition caused by limited spatial viewing of the lower atmospheric layers). The second issue is the time between images; satellites only provide one picture per day, which

is insufficient for several solar power-plant applications.

In our work, we have developed a novel system that combines satellite images, two digital cameras and the Fiat-Lux model to predict, at a sub-hourly scale, the total flux and the irradiance peak distribution on the CESA-I CSTP plant receiver located at the PSA. Specifically, the METEOSAT satellite images were used to predict the DNI at the CESA-I emplacement, the two digital cameras provided the real *Extinction* value (measured in-situ at the PSA site) and the Fiat-Lux model determined the total reflected power and the peak of irradiance on the receiver placed on top of the CESA-I tower.

2. Experimental data

The complete development of the system to determine DNI forecasting in the solar-tower plant receiver was carried out at the Plataforma Solar de Almería, where different strategies and systems were combined in order to maximize knowledge regarding the atmospheric attenuation involved in the pathway between the heliosats and the receiver.

2.1. Solar field features

In order to have a better representation about the solar field modelled in this work, a complete explanation is presented. The idea is to consider this solar field as reference to test the importance of several factors involved in the plant operation, including the energy potential forecasting. Moreover, having the solar field's technical data, it would be possible to scale and reproduce the method to other solar fields. The installation captures direct solar radiation using a field of 300 heliostats, each with a surface area of 39.6 m^2, distributed in a northern field of 16 rows covering an extension of 330 x 250 m. The receiver is a 2.2 x 2.6 m^2 volumetric receiver composed by 270 individual absorbers made of SiC (silicon carbide) ceramic material. The nominal thermal power of the receiver is 3 MW. The heat transfer fluid employed in the receiver is atmospheric air at 850 ^{o}C of nominal temperature. Fig. 1 shows a picture of the solar field.

Interesting measurements of the solar field are: the distance between the central tower and the first row of heliostats is 45 m; with the farthest row 259 m, and the maximum width of the solar field is 312 m. The heliostats have an average nominal reflectivity of 90%, the solar tracking error on each axis is 1.2 mrad and the reflected beam image quality is 3 mrad. Despite

Figure 1: Aerial view of the solar tower power plant at PSA.

being more than 20 years old, the heliostat field is in an optimal operational state as it has been strategically maintained by replacing mirrors and facets and repairing drive mechanism components. To the north of the heliostat field, there are two additional areas that are used as a test platform for new heliostat prototypes, one located 380 m from the tower and the other 500 m away. The maximum thermal power that the field provides over the receiver opening is 7 MW; at a typical design irradiance of 950 Wm^{-2}, a peak flow of 3.3 MWm^{-2} is achieved. Ninety nine percent of the power is collected in a

circle with a 4 m diameter, and 90% of this is in a 2.8 m circle diameter. The hot air of the receiver can be either directed to a steam generator to drive a Rankine thermodynamic cycle; or conducted through a rock packed bed thermal storage. This thermal storage is made of 12 tons of small alumina pieces with a total thermal power of 1MWh.

The tower is made of concrete and is 80 m height. It can support a 100-ton load. In the tower, there are three testing levels: at 45 m height, there is a cavity adapted to use as a solar furnace and to test materials, which has been employed to reproduce the heating ramp that exists on re-entry into the atmosphere, to test the ceramic pieces of space shuttle shields and used in the surface treatment of steels and other metal compounds. There is also cavity with a calorimetric test bench of volumetric receivers pressurized to 60 m whereas in the upper part of the tower, at a height of 80 m, there is a test installation for atmospheric volumetric receivers. On top of the tower, there is a crane with a 5-ton capacity and a forklift with a 1000 kg capacity.

2.2. Meteorological station description and radiation data

For this study, the meteorological station located in the CESA building was used. It has a two-axe solar tracker ($2APKipp$ & $Zonen$) above which direct, global and diffuse horizontal irradiance are measured. Additionally,

we have an image reception system from the Meteosat Second-Generation (MSG) satellite located in the CIESOL building at the University of Almería.

For the radiation forecasting, MSG satellite channels were collected every 15 minutes throughout 2017. For the DNI prediction, two computers were employed. The first one collects the satellite channels in real time, for where there are no special operating system requirements. The second computer (Intel(R) Core (TM) i7-3537U CPU @ 2.00 GHz with an 8.00 GB RAM memory) processes the images and executes the algorithm designed to obtain the final forecasting. In this case, the OS should be 64 bits and MATLAB must be installed as the development environment. These computer specifications guarantee that the efficiency of each iteration's execution is the lowest because, under 64 bits, the advantage of the total RAM size along with an octa core means that the workload is evenly distributed. After obtaining three consecutive images, the average time spent for one 2-h forecast is less than 4 seconds.

3. Methodology

This section describes the different tasks used to define the methodology and processes carried out to predict the energy flux distribution in the central

solar power plant receiver. The section is divided into different subsections according to the thematic involved in each process. In order to have a global view about the process to predict the power flux on the central tower receiver, Fig. 2 shows a flowchart with the main steps.

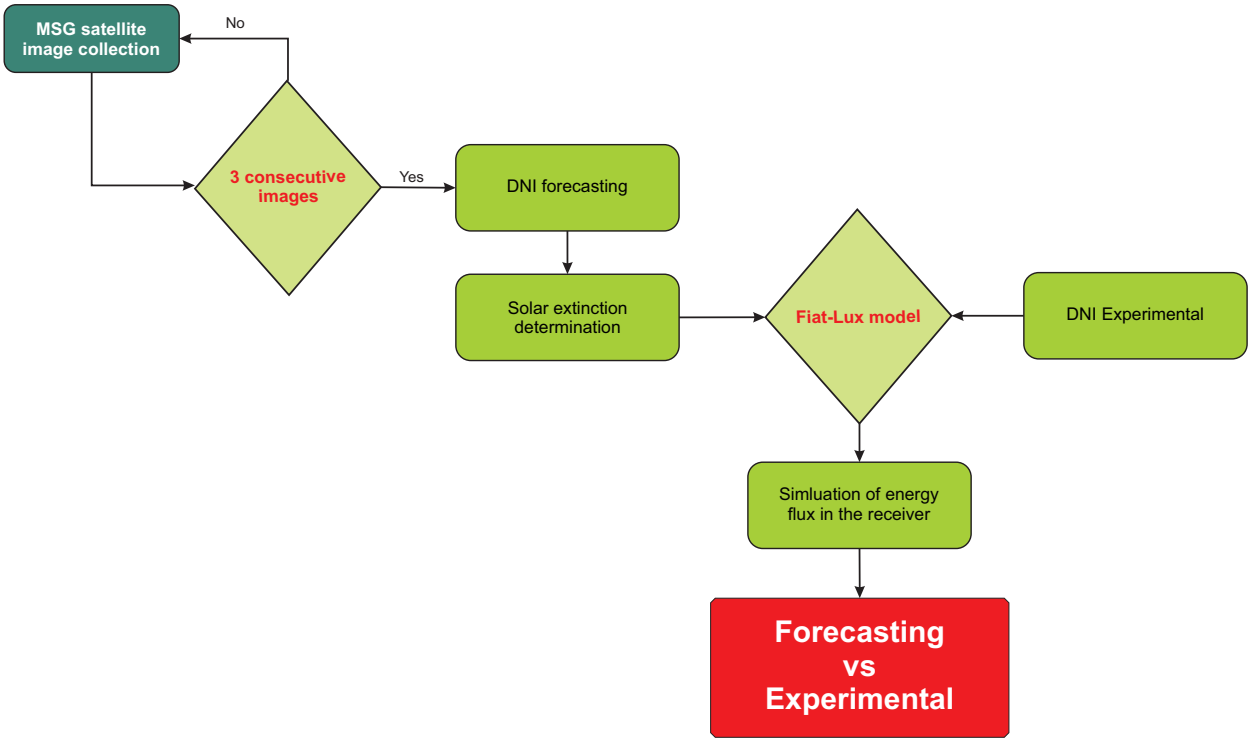

Figure 2: Sequence of steps for determining the flux forecasting in the receiver of the CESA tower plant.

The first step consists on having three consecutive MSG images, centered in the PSA, to provide the DNI forecasting. Subsequently, the solar extinction is calculated in the PSA emplacement. After that, the DNI is included in the Fiat-Lux model to obtain the energy flux simulation in the receiver of

the power tower plant. At this point, two calculations are performed: one of them by including the extinction, and another one without it. In parallel, the Fiat-Lux model receives the measured DNI value, for the predicted time, also in order to calculate the simulation of the energy flux. Finally, the results are compared in order to obtain the best accuracy.

3.1. Detection and motion of clouds

The first step in carrying out solar radiation forecasting is to correctly collect the satellite images. The MSG takes pictures of the Earth every 15 minutes over 11 spectral channels with a 3-km resolution at nadir and one high-resolution vision channel with a 1-km resolution. For cloud detection, only five channels are used; these are listed in Table 1.

Table 1: Meteosat channels used for the cloud detection.

Channel name	Wavelength (μm)
VIS 0.6	0.635
VIS 0.8	0.81
IR 3.9	3.90
IR 10.8	10.80
IR 12.0	12.00

The received images are reduced by taking a 121x161 pixel raster image centered on the Plataforma Solar de Almería (PSA). After that, an algorithm

used to detect the presence of any clouds is applied to the various atmospheric layers of the raster map, considering the full raster image [28]. With the cloud detection carried out in the three consecutive images, the cloud motion vectors are determined.

When clouds are detected in the three images (over 45 minutes, with one image every 15 minutes), each image is divided in five sectors for better motion definition. The Maximum Cross Correlation (MCC) method is applied to each sector between the first and second raster images, and between the first and third images, producing a pixel maximum between each pair of two consecutive images where they are most similar [29, 30]. This maximum describes the pixel motion and, consequently, the cloud motion. Following this, six quality tests (to delete erroneous, invalid or incoherent vectors) are applied to the vectors to choose the cloud tracking vector. Accordingly, the wind vectors are defined for each sector, supposing one displacement for a 15-minute period. Using this condition, each motion represents the future cloud position and, therefore, the future positions of the pixels [31, 32].

3.2. DNI forecasting from MSG imagery

To consider all the possible sky types, the Heliosat2 algorithm is applied, which works using Meteosat images as the input data. Basically, this method

considers the DNI estimation under cloudless skies and then applies an attenuation factor determined by the presence of clouds. The expression which represents this approach is defined by Eq. 1:

$$DNI = DNI_{cless} \;\; k_{cs} \tag{1}$$

where DNI_{cless} is the direct normal irradiance in Wm^{-2} for cloudless skies; and k_{cs} is the attenuation factor.

The value of DNI_{cless} is calculated in the last raster image, simulating that the atmosphere is clear of clouds. For this, the ESRA model was used as one of the most extended and validated solar radiation estimation models under clear skies by using satellite images [33], as shown in Eq. 2:

$$DNI_{cless} = I_0 \varepsilon T_{rb}(\alpha) \tag{2}$$

where I_0 is the solar extraterrestrial radiation, ε is the correction used for the variation in the sun-earth distance from its mean value and $T_{rb}(\alpha)$ is represented as a function of the α (solar altitude angle), and is calculated using Eq. 3:

$$T_{rb}(\alpha) = \exp(-0.8662 T_L m \delta_R(m)) \tag{3}$$

where T_L is the Linke turbidity factor, defined as the number of clean and dry atmospheres needed to achieve the observed level of attenuation, basically comprising the attenuation caused by aerosols and water vapor combined; m is the air mass and $\delta_R(m)$ is the Rayleigh optical thickness.

When DNI_{cless} is obtained for cloudless skies, the last step for estimating the DNI value is to obtain the k_{cs} value. To do this, the Heliosat-2 method is used, a model which employs satellite images to calculate atmospheric attenuation [34, 35]. As with the DNI_{cless} estimation, the Heliosat-2 model is applied to the last satellite image, considering the ground apparent albedo, the minimal ground albedo and the cloud albedo. In this way, two matrices are obtained; one representing the DNI_{cless} estimations at pixel level and the other representing the k_{cs} factors, also at the pixel level. Given that cloud motion defines the motion of the pixels, every displacement of the k_{cs} matrix represents a 15-minute prediction for each motion, so 8 motions are practiced to obtain a forecast from 15 to 120 minutes.

Therefore, to calculate the DNI for the subsequent two hours, when the k_{cs} pixels are moved, the DNI_{cless} is estimated for the future moments and

for a cloudless sky in all the pixels of the satellite raster image [26], ending with the product between the DNI_{cless}, estimated in a pixel, and the k_{cs}, in the same pixel, thus generating the final DNI forecast. To understand this process better, Figure 3 represents the matrices with the satellite estimations for cloudless skies depending on the emplacement described by each pixel (3-A) and the k_{ci} indexes (3-B). Each pixel of each matrix is moved according to the cloud motion vectors and, finally, the product of the two matrices determines the predicted DNI value at PSA (the central pixel of each matrix marked in red) [36].

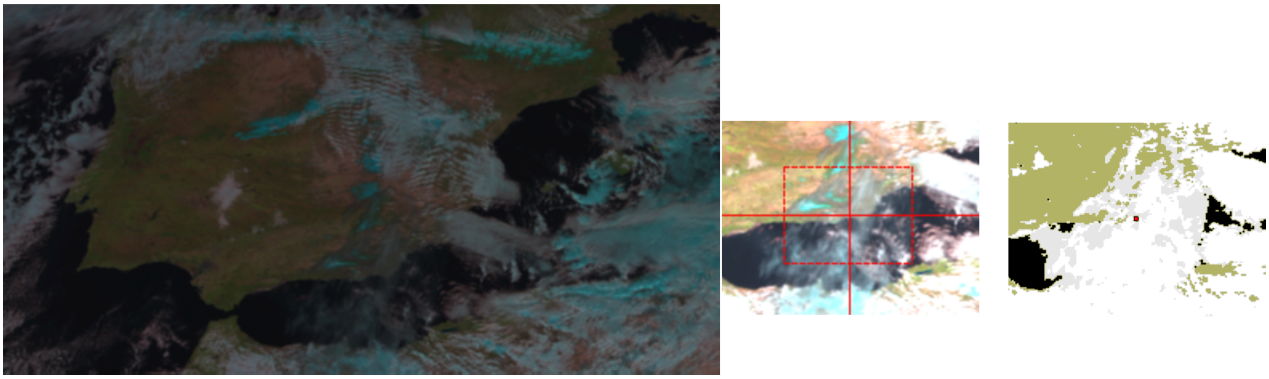

Figure 3: Satellite vision for a particular moment studied in the PSA site.

3.3. Determination of the attenuation coefficient

To determine the attenuation coefficient, a novel system was implemented [27]. The aim of this measurement system is to take simultaneous images of

the same target at different distances using two identical optical systems based on digital cameras, (Hamamatsu, model ORCA-flash4.0 v3 CMOS) using suitable lenses and filters.

The distances from the cameras to the center of the target were chosen as 82.88±0.01 m and 824.51±0.01 m, so that the target area projected per pixel is similar in both cameras (10.4 mm in diameter for the nearest camera and 11.2 mm for the farthest). With this procedure, it is necessary to work with the diffuse solar radiation reflected by the target in order to avoid the direct solar radiation; thus minimizing specular influences and directionality. The spectral range of the cameras is focused between 400 and 1000 nm. The target has a Lambertian surface with dimensions of 2 x 2 m. Two standard 2 x 1 m steel plates were used for its construction: one painted white (Amercoat741) and the other one in Zynolyte black to avoid the air light in the measurements [37]. Figure 4 shows the scheme for this novel attenuation coefficient determination using digital cameras.

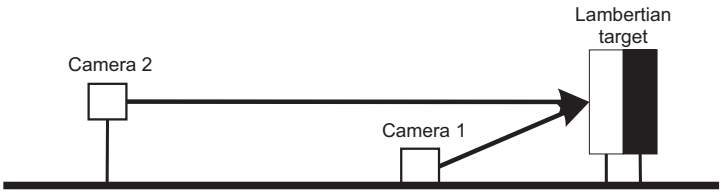

Figure 4: General scheme for the configuration of cameras and Lambertian target in the PSA emplacement.

Each camera is connected to a laptop integrated into a customized box with programmed refrigeration. The cameras take an image focusing on the Lambertian target. The attenuation is determined by comparing the two images, following Eq. 4:

$$Extinction\ (\%) = 100\left(1 - \frac{I_2}{I_1}\right), \tag{4}$$

where I_1 (I_1=I_{1W}-I_{1B}) and I_2 (I_2=I_{2W}-I_{2B}) are the average intensities of the images.

Moreover, the system has a minimizing noise reduction system, taking 20 images in less than a second. With this process, the images are well defined for characterizing the final atmospheric attenuation value. As the *Extinction* obtained is for the distance between the cameras (741.63 m), we need to apply the *Extinction* coefficient for the distance of each heliostat to the central tower. Accordingly, we applied the Beer-Lambert-Bouguer law to rescale the *Extinction* from 741.63 m to 140 m, which is the average distance from the heliostats to the receiver. To accomplish this, the *Extinction* coefficient (β_{Ext}) can be derived from the Beer-Lambert-Bouguer law, following Eq. 5:

$$\beta_{Ext} = -\frac{ln\frac{I_2}{I_1}}{D}, \tag{5}$$

where D is the distance between cameras (741.63 m).

The *Extinction* for a given distance (D) can now also be determined in relation to previous expressions using the same law, concluding with the general expression provided by Eq. 6:

$$Extintcion(D) = 1 - e^{-\beta_{Ext}D}, \tag{6}$$

As the *Extinction* calculation methodology is applied to the distance between the cameras, set at 741.63 meters, the next step consists on extrapolating the *Extinction* to the distance from the heliostats to the receiver at the top of the central tower. Considering a (β_{Ext}) common to the surroundings of the measurement emplacement of the cameras (near to the CESA-I PSA solar field), we can calculate the *Exctinction* coefficient for the *Exctinction* obtained from the cameras by clearing this variable, as shown by Eq. 7:

$$\beta_{Ext} = \frac{ln(1 - Extinction(D))}{D}, \tag{7}$$

When the extinction coefficient (β_{Ext}) is calculated, we can use expression

6 to consider the new distance of 140 meters (the average distance from the CESA-I PSA solar field heliostats to the central receiver). Consequently, the extinction for the new distance is obtained and included in the DNI forecasting methodology, decreasing the predicted DNI, which will serve as the input for the flux prediction method (Fiat-Lux).

3.4. Flux prediction on the central tower receiver

When the DNI has been predicted, the optical losses are computerized. For this, the flux (in Wm^{-2}) for the tower receiver (located 82 meters above ground level) is predicted by using the predicted DNI data and the Fiat-Lux model [38]. The Fiat-Lux code is based on the precise knowledge of the sun-shape image, which is captured by a 14-bit resolution CCD imaging device and transformed into a representative matrix of the spatial distribution of the sun's intensity. Therefore, the sun's trajectory from a reference heliostat, also located at the PSA site, has been studied. This heliostat was selected from the CESA-I PSA solar field; it consists of a 39.9 m^{-2} twelve-facet heliostat with a focal distance of 260 m and a solar weighted reflectance of 0.94.

The first step in the Fiat-Lux model is to define the sun's reflection on a single mirror. Subsequently, a CCD camera, picture acquisition and the PROHERMES processing software are used to study the sun's shape. The

sun picture is taken at the time of the test to determine the input signal properties. Furthermore, DNI measurements are acquired to provide physical measures. This is how the intensity calibration of the solar disk is performed. In addition, a spatial calibration of the sun is carried out to properly define the unitary vectors of the solar area. Once the mathematical operation of the previous steps has been done, the sun's projection is determined by taking into account the sun's current position, the mirror and the target. The final projection of the sun shape reflected by the mirror can be determined using the ray-tracing technique. The goal is to determine the conjugated image of everything related to the optics system (the mirror) on the target plane (the mirror's reflectivity, the geometrical properties of the reflecting surface, the impact point calculation on the target plane and the proper topology to manage the flux distribution as a matrix). After applying the Fiat-Lux model, an estimation of the total flux reaching the receiver is obtained.

4. Results

In this section, the results of the developed work are presented. Two totally cloudless days, separated in time, were selected in 2017, for which satellite images and attenuation data were available simultaneously. To ana-

lyze the influence of the attenuation data on DNI forecasting for the receiver located on top of the central solar power plant, we calculated the total power and the peak of irradiance on the receiver for three different scenarios depending on the DNI value used as the input: (1) by using the measured DNI, (2) by using the DNI forecasting without including the extinction at the different time-scales and (3) by using the DNI forecasting including the extinction (Eq. 4) also at the different time-scales. The total power is the incident energy flux (measured in kW). The irradiance peak is the maximum value of solar energy flux density incident on the surface of the solar receiver. This energy comes from heliostats field. Its value is estimated, by simulation, in a plane that coincides with the surface of the receiver. The objective was to determine whether results from the total reflected power and the irradiance peak using the forecasting (with/without attenuation) were more alike than when using the measured DNI values.

One important factor for characterizing the energy flux reaching the receiver is the form and size of the sunlight concentration from the heliostats. In this work, we have simulated the sun's reflection on two different random cloudless days (at different moments of the year) to observe the optical distribution on the receiver for a normalized DNI value of 1000 Wm^{-2}. All the

predictions were made at the same timescale: 15, 30, 60, 90- and 120-min. Figure 5 shows the distribution of energy in the central receiver for three different predictions on one of the studied days.

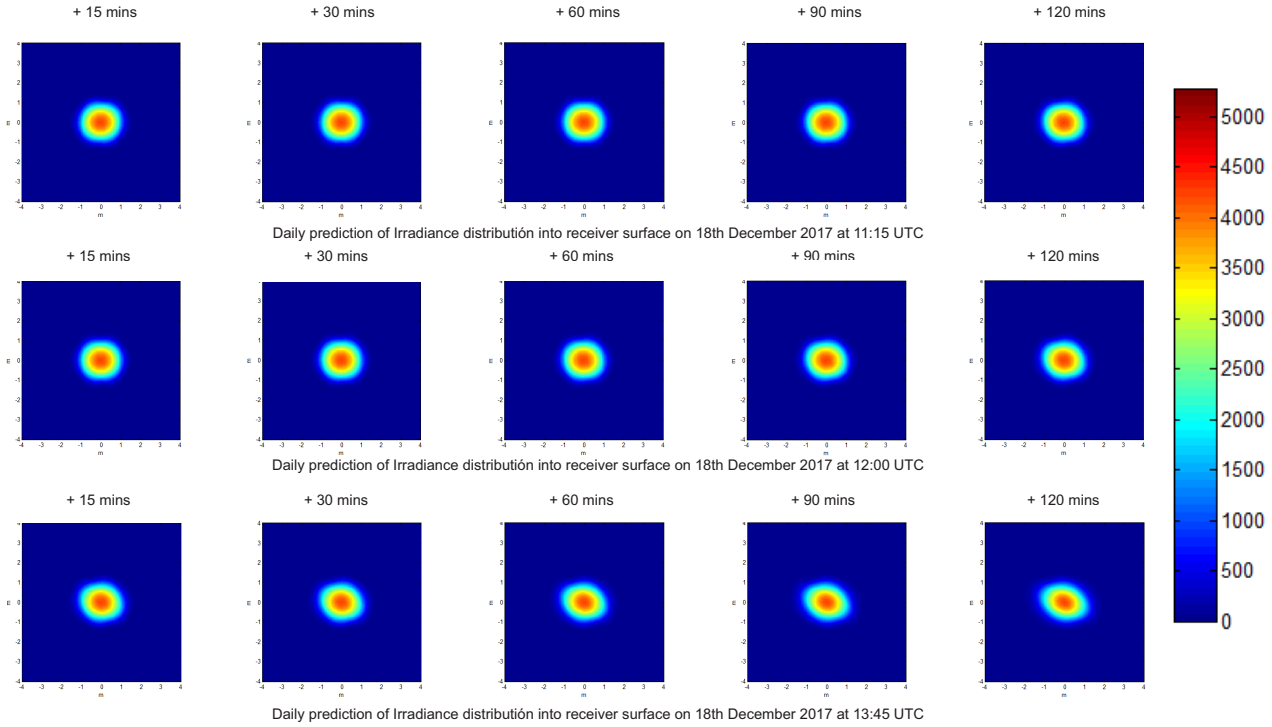

Figure 5: Optical distribution of flux in the receiver of the CESA tower plant placed at Plataforma Solar de Almería on December 2017.

Considering the nominal DNI values, we can study the variations in size and form of the irradiance distribution on the surface of the central receiver in different moments. The strong astigmatism alters the morphological characteristics of the reflection: it is elongated, and the main axes of this elongation are oriented in a predictable and concrete direction of the target. Further-

more, the low peak and the Gaussian distribution deform considerably. This specific form of flow distribution at that moment is invariant in the face of DNI changes. Therefore, this is the cause why, in this study, the irradiance distribution is determined by a nominal DNI value. Knowing this, we can see that the simulations present homogeneous forms in the forecasting carried out at 11:15 UTC, take a circular form in the predictions from 15 to 90 min, but are different in the last prediction (120 min). The same behavior is presented in the following predictions, where the focus of the heliostats' projected power represents an oval form. Mainly, this feature results from the time of the day. As one can see, time is important as to the form of the irradiance distribution in the rest of the predictions (12:00 and 13:45 UTC), the aspect of the flux distribution varies. This is mainly caused by the effect of the sun's position, which presents a different morphology at noon than at other times of the day. At these moments, the average extinction value was 3.8%, which is not so much compared with some of the dust events. For this reason, Table 2 shows the main aspects involved in the simulation of the flux distribution on the target.

In the previous table, the air mass, the azimuth and the elevation angles were calculated for each prediction. P_E on target (in kW) and E_{peak} (in

Table 2: Data of predictions carried out on 18 December 2017 in the CESA tower placed at Plataforma Solar de Almería.

Time (UTC)	Prediction	Azim. (^{o})	α (^{o})	m	P_E (kW)	E_{peak} (kWm^{-2})	DNI_{fore} (Wm^{-2})
11:15	+15 min	9.47	28.94	2.062	10672.67	4227.77	981.50
	+30 min	5.56	29.33	2.037	10690.93	4238.29	984.72
	+60 min	-2.34	29.50	2.027	10698.54	4243.05	986.04
	+90 min	-10.18	28.84	2.068	10667.57	4224.83	980.58
	+120 min	-17.81	27.40	2.168	10598.25	4188.63	967.89
12:00	+15 min	-2.34	29.50	2.027	10698.54	4243.05	986.00
	+30 min	-6.28	29.27	2.041	10687.87	4236.48	984.14
	+60 min	-14.03	28.22	2.110	10637.68	4206.02	975.16
	+90 min	-21.50	26.39	2.244	10549.34	4161.59	958.49
	+120 min	-28.56	23.86	2.463	10423.42	4100.20	932.56
13:45	+15 min	-28.56	23.86	2.463	10423.42	4100.20	970.67
	+30 min	-31.92	22.36	2.618	10346.63	4062.32	952.73
	+60 min	-38.29	18.93	3.066	10166.09	3967.94	905.14
	+90 min	-44.18	14.99	3.828	9950.73	3837.70	835.45
	+120 min	-49.64	10.65	5.306	9702.29	3663.06	729.01

kWm^{-2}) were determined considering the nominal DNI value of 1000 Wm^{-2}. The representativeness of this table is the decreasing values of P_E and E_{peak} variables, whereas the air mass presents increasing values. This atmospheric variable reduces the DNI hitting the ground and, together with the motion of the Earth, provokes a diminution of power onto the target. However, as mentioned before, the size and form of the flux distribution is independent of the DNI amount. In general, the distribution of energy gives information about the peak power and the homogenization that occurs in the central receiver. To contrast this day with one in a different season, we chose the 30th June 2017. Figure 6 shows the optical properties of the simulations for the selected day.

In this case, the optical properties present a different size and form than the predictions for December (Fig. 5). One can appreciate that non-circular

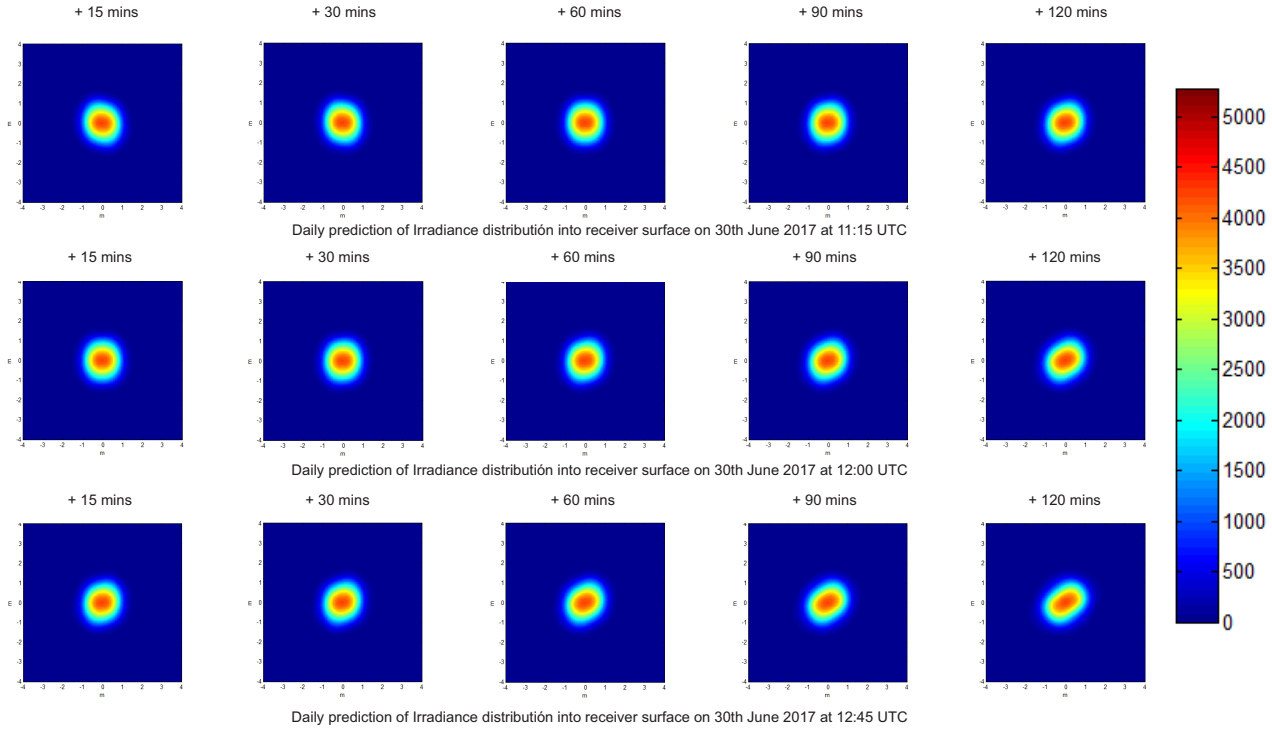

Figure 6: Optical distribution of irradiance in the receiver of the CESA tower plant placed at Plataforma Solar de Almería on June 2017.

forms are obtained in the flux projection simulation, with the cases nearest to sunset deforming especially. For these, the sun position means that the heliostat mirrors do not concentrate the sunlight in a homogeneous and perfect circle, resulting in an elliptical form, less desirable for a perfect reflection. Curiously, the average extinction value for this day was 6.3%, much greater than in December. Table 3 shows the main characteristics for the flux distribution simulation on the target in June.

In this table, we can see that the sun's projection from the heliostats

Table 3: Data of predictions carried out on 30 June 2017 in the CESA tower placed at Plataforma Solar de Almería.

Time (UTC)	Prediction	Azim. (^{o})	α (^{o})	m	P_E (kW)	E_{peak} (kWm^{-2})	DNI_{fore} (Wm^{-2})
	+15 min	36.65	73.25	1.044	9872.94	3766.37	999.26
	+30 min	25.43	74.80	1.036	9886.18	3786.07	1002.53
11:15	+60 min	-1.75	76.50	1.030	9904.16	3801.63	1003.87
	+90 min	-28.36	74.46	1.017	9892.08	3783.59	998.32
	+120 min	-47.93	70.73	1.059	9826.52	3724.04	985.40
	+15 min	-1.75	76.05	1.030	9915.82	3801.63	1006.56
	+30 min	-15.72	75.59	1.032	9909.19	3798.82	1004.65
12:00	+60 min	-39.09	72.80	1.046	9864.52	3757.64	995.49
	+90 min	-55.18	68.39	1.075	9778.12	3678.38	978.47
	+120 min	-66.22	63.16	1.017	9650.36	3552.49	952.01
	+15 min	-39.09	72.80	1.046	9864.52	3757.64	1024.27
	+30 min	-47.93	70.73	1.059	9826.52	3724.04	1005.34
12:45	+60 min	-61.18	65.85	1.096	9719.38	3619.94	955.13
	+90 min	-70.53	60.38	1.017	9571.13	3469.83	881.59
	+120 min	-77.63	54.63	1.226	9382.44	3274.47	769.93

to the central tower is mainly affected by the cosine effect in the reflection process. Knowing that the DNI does not vary in the simulation with a nominal irradiance of 1000 Wm^{-2}, the sun's position plays an important role as the main factor for decreasing P_E onto the target and E_{peak}. In this case, P_E is always lower than 10000 kW and the E_{peak} presents values lower than 4000 kWm^{-2}. Consequently, knowing the flux distribution on the target, we can determine the optical properties of the heliostats' refraction and the power that reaches the tower receiver. For calculating the real values of P_E onto the target and E_{peak} according to real or predicted DNI values (including/not-including extinction), it is necessary to convert the nominal result values to real episodes, following Eqs. (8, 9).

$$Real\ P_E\ (kW) = \frac{DNI_{fore}}{1000}\ P_E\ (for\ 1000\ Wm^{-2}), \tag{8}$$

where $\mathrm{DNI}_{fore.}$ is the DNI value predicted using MSG satellite images (Wm^{-2}), 1000 is the nominal DNI used (Wm^{-2}), and P_E on target (for 1000 Wm^{-2}) is the output of the Fiat-Lux model simulation (kW).

$$Real\ E_{peak}\ (kWm^{-2}) = \frac{DNI_{fore}}{1000} E_{peak}\ (for\ 1000\ Wm^{-2}), \tag{9}$$

where E_{peak} (for 1000 Wm^{-2}) is the output of the Fiat-Lux model simulation (kWm^{-2}).

With these conversions, we obtain the real values of P_E and E_{peak} onto the target. However, this work also includes a DNI attenuation factor as an extinction measurement. To discern the best approach, we contemplated two scenarios: a DNI forecasting including and not including the extinction at 140 meters. Therefore, with these two options, we obtained the predictions for P_E onto the target and E_{peak} for the scenarios mentioned before, and for the case in which we use the real DNI values. This allowed us to compare the predictions with the experimental data. Hence, in the common graphs, the two predictions were compared with the real data from all the predictions. Fig. 7 shows the comparisons with the day analyzed on 18 December 2017.

In the figure, there is one graph for each prediction and for each variable analyzed. In the left column, P_E predictions appear at 11:15, 12:00 and 13:45

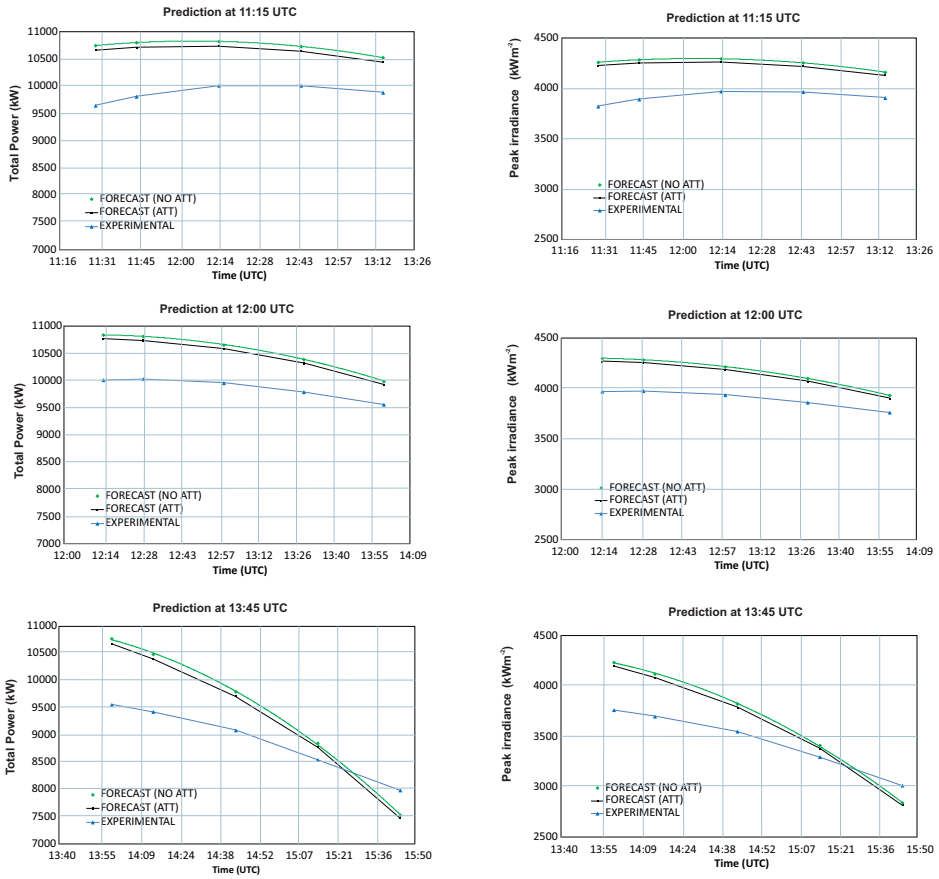

Figure 7: Representation of the predictions for P_E and E_{peak} in the receiver of the CESA tower plant placed at Plataforma Solar de Almería on December 2017.

UTC. The right column represents E_{peak} predictions during the same periods. In all the graphs, the blue lines represent the real measurements; the black lines represent the predictions including the extinction in the DNI forecasting, whereas the green lines are used to illustrate the forecasting without the extinction. The first characteristic is the behavioral similitude in the curves between P_E and E_{peak}. Generally, the predicted variables are overestimated

in all cases except the last prediction (13:45), where the forecasting is underestimated at 14:45 UTC. Therefore, in most cases, the extinction causes a better fit in the prediction because the extinction is considered as a decrease in predicted values. In the case of June, Fig. 8 shows the corresponding graphs:

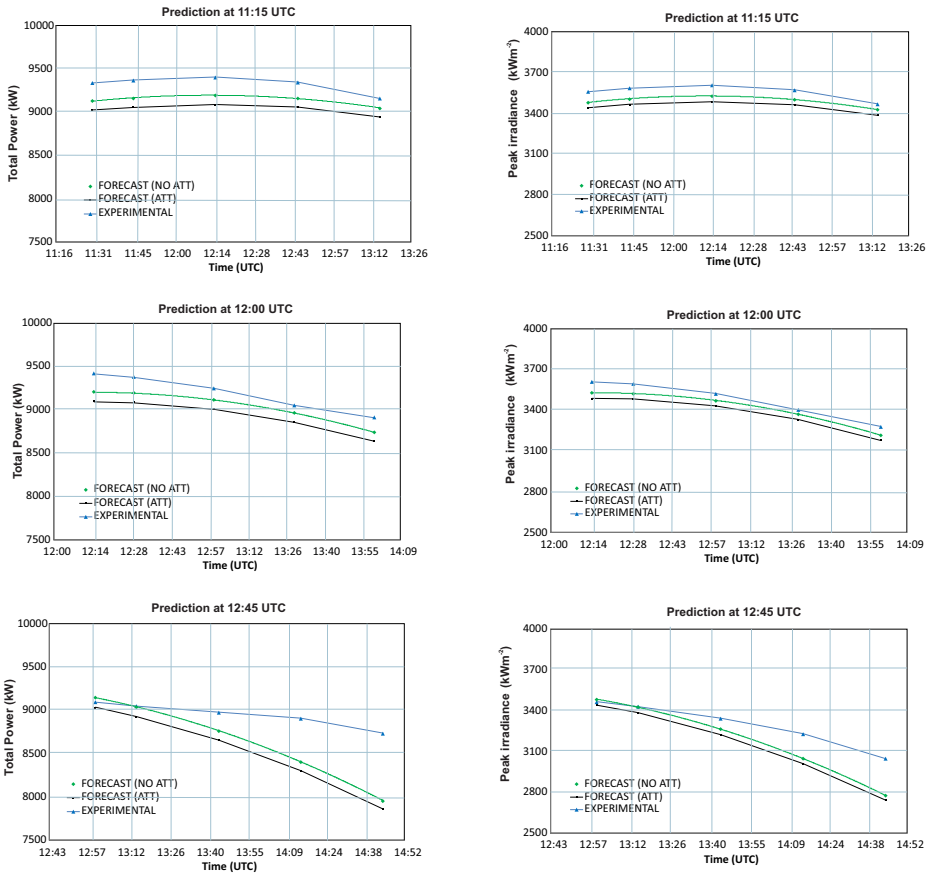

Figure 8: Representation of the predictions for P_E and E_{peak} in the receiver of the CESA tower plant placed at Plataforma Solar de Almería on June 2017.

In these situations, it is representative that the two predictions (including

and not including extinction) are very near to the real values for all cases. This is a result of the accuracy of the DNI forecasting method, which presents a good fit between the forecasting and experimental data. The prediction carried out at 12:45 underestimates P_E and E_{peak} values in the predictions between 13:45 and 14:45 UTC. Normally, this underestimation is because of the decreasing solar altitude. In cloudless skies, the DNI establishes a maximum at midday, with constant values existing for a few hours; however, when the sun starts to go down, the DNI decreases more quickly, which is far harder to predict one or two hours beforehand. Moreover, it has be found that this day, the average extinction was placed in a value of 6.3%, whereas in December it was placed at 3.8%. This fact has allowed us to suppose that the high extinction has been interpreted like a light cloud, decreasing the DNI forecasting.

In order to obtain more details regarding the experimental data compared to the predicted values, we calculated the correlation coefficient in all the scenarios (Eq. 10), considering that $\sigma_{X_{est,mea}}$ is the covariance of the two inputted data sets [the predicted and measured values (X_{est} and X_{mea}, respectively)], $\sigma_{X_{est}}$ is the standard X_{est} deviation and $\sigma_{X_{mea}}$ is the standard X_{mea} deviation.

$$R = \frac{\sigma_{X_{est}X_{mea}}}{\sigma_{X_{est}}\sigma_{X_{mea}}} \tag{10}$$

Fig. 9 shows the dispersion graphs and the correlation coefficient for the predictions, according to Eq. 10.

In general, according to the graphs, it is not difficult to see the good fit in all cases. The R coefficient presented a value of 0.97 when comparing the real values with the predictions, both with and without extinction, with values of 0.95 and 0.99 for June and December, respectively. In the case of E_{peak}, the R coefficients were also calculated (by using Eq. 10) and the graphs are shown in Fig. 10.

As occurred with P_E predicted onto the receiver, the R coefficient presented very good values. Analyzing each day, the results are very similar to those predictions using and not using the extinction in the DNI forecasting, with the same behavior in all cases. In general, when combining the two days used for this study (in December and June), the R coefficient is always higher than 0.95. Moreover, we have used two more statistical variables, widely employed in these works: the normalized root mean square and mean bias errors. The first shows the dispersion of the experimental data and is defined by Eq. 11:

$$nRMSE(\%) = \frac{100}{\overline{X}} RMSE \tag{11}$$

where $\overline{X}$ is the average of measured values and RMSE is the root-mean square error defined by Eq. 12.

$$RMSE = \sqrt{\frac{1}{N}\sum_{i=1}^{N}(X_{est} - X_{mea})^2} \tag{12}$$

where N is the amount of data.

Subsequently, the normalized Mean Bias shows the trend above the experimental data underestimation and is expressed by Eq. 13:

$$Normalized\ Mean\ Bias\ (\%) = \frac{100}{\overline{X}} Mean\ Bias \tag{13}$$

where Mean Bias is defined by Eq. 14.

$$Mean\ Bias = \frac{\sum_{i=1}^{N}(X_{est} - X_{mea})}{N} \tag{14}$$

Following the above expressions, Table 4 shows the results of these statistical errors.

Both nRMSE and nMBE values present good results for the simulation

Table 4: Statistical errors for the prediction of P_E and E_{peak} for the cases analysed at Plataforma Solar de Almería.

	nRMSE (%)	**nMBE (%)**
P_E on target (no extinction)	5.99	-1.87
P_E on target (extinction)	5.90	-0.87
E_{peak} (no extinction)	4.89	0.21
E_{peak} (extinction)	5.08	1.32

process. For nRSME, the values are below 6% in P_E prediction, slightly better when the extinction is included.

This result is also applied to the nMBE, where the predicted value using the extinction is underestimated in less than 1%. If E_{peak} is analyzed, the pattern follows an opposite trend, i.e. the results are a little better when the extinction is not used. However, the extinction supposed for this work was for a distance of 140 meters. If this work had been elaborated in a commercial solar power plant with greater distances between the heliostats and the central tower, the results would clearly have been better when including the extinction in the DNI forecasting.

Therefore, we have reported on an exhaustive analysis of the flux simulation in a real central solar-tower power plant, in which Meteosat satellite DNI predictions were combined with extinction as an attenuating factor to model the behavior of P_E and E_{peak} onto the CSTP plant receiver.

5. Conclusions

In this work, we have developed a methodology that integrates a DNI forecasting method based on satellite images (from 15 to 120 minutes) with an attenuation factor provided by a novel system of two digital cameras which determines the extinction. This integration was used as the input for a solar power plant simulation model (Fiat-Lux) to ascertain the total reflected power and E_{peak} reaching the receiver of the CESA-I tower located at the Plataforma Solar de Almerá.

The total power and the irradiance peak were predicted on the CESA-I tower receiver using the DNI values predicted with satellite images. These predictions were compared with real data. When the attenuation factor was included in the DNI forecasting, the nRMSE was lower than 6% in P_E, and higher than 5% in E_{peak}. If the attenuation factor is not included in the DNI forecasting, E_{peak} presents better results with an nRMSE value of 4.89% and an nMBE value of 0.21%.

The correlation coefficient was calculated for the comparison between P_E by using and not the attenuation factor. In general, the results show an R value higher than 0.94 in all cases, presenting the best adjustment between P_E estimated and predicted by including the attenuation factor, with a value

of 0.992.

In conclusion, we have presented a proper prediction control system for the flux distribution in the central receivers of CSP plants, which contributes for studying the effects altering the sunlight trajectory between the heliostats and the receiver, and, therefore, to ensure the efficient and safe operation of solar tower systems.

6. Outlook and future works

This article is a starting point for combining methodologies that predict solar power plant potential by including remote sensing techniques, digital cameras and simulation models. In any future work, it would be a good idea to compare different extinction models (i.e. based on satellite information or using other sensors) to determine the best option in order to obtain a more accurate extinction value, including DNI forecasting. Moreover, artificial intelligence techniques might be a good choice in this area to compare with the simulations carried out in our work. To determine the importance of this prediction system in an experimental solar power plant, one needs to extend the knowledge acquired from a commercial CSTP plant that employs greater distances between the heliostats and the central receiver (reaching longer

than one kilometer distances), where extinction losses are more considerable and the results might be different.

7. Acknowledgements

The authors would like to thank the PRESOL Project (references ENE201459454-C3-1, 2 and 3) and the PVCastSOIL Project (ENE2017-83790-C3-1, 2 and 3), which were funded by the *Ministerio de Economía y Competitividad* and co-financed by the European Regional Development Fund. The authors also acknowledge the financial support provided by the Innova-Chile program of the Chilean Economic Development Agency, CORFO (with project code: 17BPE3-83761) and CONICYT/FONDAP/15110019 "Solar Energy Research Center" SERC-Chile

References

[1] N. Yamani, A. Khellaf, K. Mohammedi, O. Behar, Assessment of solar thermal tower technology under algerian climate, Energy 126 (2017) 444–460.

[2] Z. Zhu, D. Zhang, P. Mischke, X. Zhang, Electricity generation costs

of concentrated solar power technologies in china based on operational plants, Energy 89 (2015) 65–74.

[3] S. Mihoub, A. Chermiti, H. Beltagy, Methodology of determining the optimum performances of future concentrating solar thermal power plants in algeria, Energy 122 (2017) 801–810.

[4] A. Fritsch, R. Uhlig, L. Marocco, C. Frantz, R. Flesch, B. Hoffschmidt, A comparison between transient cfd and fem simulations of solar central receiver tubes using molten salt and liquid metals, Solar Energy 155 (2017) 259–266.

[5] A. Starke, L. Lemos, J. Boland, J. Cardemil, S. Colle, Resolution of the cloud enhancement problem for one-minute diffuse radiation prediction, Renewable Energy 125 (2018) 472–484.

[6] S. Miller, M. Rogers, J. Haynes, M. Sengupta, A. Heidinger, Short-term solar irradiance forecasting via satellite/model coupling, Solar Energy 168 (2018) 102–117.

[7] D. Kaskaoutis, A. Rashki, U. Dumka, A. Mofidi, H. Kambezidis, B. Psiloglou, D. Karagiannis, K. Petrinoli, A. Gavriil, Atmospheric dynamics associated with exceptionally dusty conditions over the eastern

Mediterranean and Greece in March 2018, Atmospheric Research 218 (2019) 269–284.

[8] J. Alonso-Montesinos, J. Barbero, J. Polo, G. López, J. Ballestrín, F. Batlles, Impact of a Saharan dust intrusion over southern Spain on DNI estimation with sky cameras, Atmospheric Environment 170 (2017) 279–289.

[9] J. Ballestrín, A. Marzo, Solar radiation attenuation in solar tower plants, Solar Energy 86 (1) (2012) 388 – 392.

[10] N. Hanrieder, S.Wilbert, R. Pitz-Paal, C. Emde, J. Gasteiger, B. Mayer, J. Polo, Atmospheric extinction in solar tower plants: Absorption and broadband correction for MOR measurements, Atmospheric Measurement Techniques 8 (8) (2015) 3467 – 3480.

[11] G. López, C. A. Gueymard, J. L. Bosch, I. Rapp-Arrarás, J. Alonso-Montesinos, I. Pulido-Calvo, J. Ballestrín, J. Polo, J. Barbero, Modeling water vapor impacts on the solar irradiance reaching the receiver of a solar tower plant by means of artificial neural networks, Solar Energy 169 (2018) 34 – 39.

[12] J. Barbero, J. Alonso-Montesinos, F. Batlles, J. Polo, G. López,

J. Bosch, J. Ballestrín, M. Carra, J. Fernández-Reche, Evolution of the aerosol extinction coefficient at 100 m above ground during an episode of Saharan dust intrusion as derived from data registered by a ceilometer in Almería (SE Spain), Vol. 2033, 2018.

[13] A. Cazorla, J. Andrés Casquero-Vera, R. Román, J. Luis Guerrero-Rascado, C. Toledano, V. Cachorro, J. Orza, M. Cancillo, A. Serrano, G. Titos, M. Pandolfi, A. Alastuey, N. Hanrieder, L. Alados-Arboledas, Near-real-time processing of a ceilometer network assisted with sun-photometer data: Monitoring a dust outbreak over the Iberian Peninsula, Atmospheric Chemistry and Physics 17 (19) (2017) 11861–11876.

[14] J. Polo, J. Ballestrín, J. Alonso-Montesinos, G. López-Rodriguez, J. Barbero, E. Carra, J. Fernández-Reche, J. Bosch, F. Batlles, Analysis of solar tower plant performance influenced by atmospheric attenuation at different temporal resolutions related to aerosol optical depth, Solar Energy 157 (2017) 803–810.

[15] J. Alonso-Montesinos, J. Polo, J. Ballestrín, F. Batlles, C. Portillo, Impact of DNI forecasting on CSP tower plant power production, Renewable Energy (2019) 368–377.

[16] B. L. Kistler, A user's manual for DELSOL3: a computer code for calculating the optical performance and optimal system design for solar thermal central receiver plants, Tech. rep. (1986).

[17] P. L. Leary, J. D. Hankins, A user's guide for MIRVAL—a computer code for comparing designs of heliostat-receiver optics for central receiver solar power plants, Tech. rep. (1979).

[18] M. J. Blanco, A. Mutuberria, D. Martinez, Experimental validation of Tonatiuh using the Plataforma Solar de Almería secondary concentrator test campaign data, 2010.

[19] J. Polo, J. Ballestrín, E. Carra, Sensitivity study for modelling atmospheric attenuation of solar radiation with radiative transfer models and the impact in solar tower plant production, Solar Energy 134 (2016) 219–227.

[20] J. García, Y. Soo Too, R. Padilla, A. Beath, J.-S. Kim, M. Sanjuan, Dynamic performance of an aiming control methodology for solar central receivers due to cloud disturbances, Renewable Energy 121 (2018) 355–367.

[21] O. Smirnova, T. Fend, R. Capuano, G. Feckler, P. Schwarzbözl, F. Sut-

ter, Determination of critical thermal loads in ceramic high concentration solar receivers, Solar Energy Materials and Solar Cells 176 (2018) 196–203.

[22] C. Fernández-Peruchena, M. Gastón, M. Schroedter-Homscheidt, I. Marco, J. Casado-Rubio, J. García-Moya, Increasing the temporal resolution of direct normal solar irradiance forecasted series, Vol. 1850, 2017.

[23] P. Kosmopoulos, S. Kazadzis, H. El-Askary, M. Taylor, A. Gkikas, E. Proestakis, C. Kontoes, M. El-Khayat, Earth-observation-based estimation and forecasting of particulate matter impact on solar energy in Egypt, Remote Sensing 10 (12) (2018).

[24] P. Kosmopoulos, S. Kazadzis, M. Taylor, E. Athanasopoulou, O. Speyer, P. Raptis, E. Marinou, E. Proestakis, S. Solomos, E. Gerasopoulos, V. Amiridis, A. Bais, C. Kontoes, Dust impact on surface solar irradiance assessed with model simulations, satellite observations and ground-based measurements, Atmospheric Measurement Techniques 10 (7) (2017) 2435–2453.

[25] N. Hanrieder, A. Ghennioui, A. Merrouni, S. Wilbert, F. Wiesinger,

M. Sengupta, L. Zarzalejo, A. Schade, Atmospheric transmittance model validation for CSP tower plants, Remote Sensing 11 (9) (2019).

[26] N. Hanrieder, S. Wilbert, M. Schroedter-Homscheidt, F. Schnell, D. Guevara, R. Buck, S. Giuliano, R. Pitz-Paal, Atmospheric extinction in simulation tools for solar tower plants, Vol. 1850, 2017.

[27] J. Ballestrín, R. Monterreal, E. Carra, J. Fernández-Reche, J. Polo, R. Enrique, J. Rodríguez, M. Casanova, J. Barbero, J. Alonso-Montesinos, G. López, J. Bosch, F. J. Batlles, A. Marzo, Solar extinction measurement system based on digital cameras. application to solar tower plants, Renewable Energy (125) (2018) 648–654.

[28] H. Escrig, F. J. Batlles, J. Alonso, F. M. Baena, J. L. Bosch, I. B. Salbidegoitia, J. I. Burgaleta, Cloud detection, classification and motion estimation using geostationary satellite imagery for cloud cover forecast, Energy 55 (2013) 853–859.

[29] J. A. Leese, C. S. Novak, V. R. Taylor, The determination of cloud pattern motions from geosynchronous satellite image data, Pattern Recognition 2 (4) (1970) 279–292.

[30] J. Schmetz, K. Holmlund, J. Hoffman, B. Strauss, B. Mason, V. Gaert-

ner, A. Koch, L. Van De Berg, Operational cloud-motion winds from meteosat infrared images, Journal of Applied Meteorology 32 (7) (1993) 1206–1225.

[31] J. Alonso-Montesinos, F. J. Batlles, Short and medium-term cloudiness forecasting using remote sensing techniques and sky camera imagery, Energy 73 (2014) 890–897.

[32] J. Alonso, A. Ternero, F. J. Batlles, G. López, J. Rodríguez, J. I. Burgaleta, Prediction of cloudiness in short time periods using techniques of remote sensing and image processing, Energy Procedia 49 (2013) 2280–2289.

[33] C. Rigollier, O. Bauer, L. Wald, On the clear sky model of the ESRA - European Solar Radiation Atlas - with respect to the Heliosat method, Solar Energy 68 (2000) 33–48.

[34] C. Rigollier, M. Lefvre, L. Wald, The method Heliosat-2 for deriving shortwave solar radiation from satellite images, Solar Energy 77 (2004) 159–169.

[35] J. Alonso-Montesinos, F. J. Batlles, J. L. Bosch, Beam, diffuse and

global solar irradiance estimation with satellite imagery, Energy Conversion and Management 105 (2015) 1205–1212.

[36] J. Alonso-Montesinos, F. J. Batlles, Solar radiation forecasting in the short- and medium-term under all sky conditions, Energy 83 (2015) 387–393.

[37] J. Ballestrín, E. Carra, R. Enrique, R. Monterreal, J. Fernández-Reche, J. Polo, M. Casanova, J. Barbero, A. Marzo, Diagnosis of a lambertian target in solar context, Measurement 119 (2018) 265–269.

[38] R. Monterreal, A new computer code for solar concentrating optics simulation, Journal De Physique. IV: JP 9-3 (1999) 77–82.

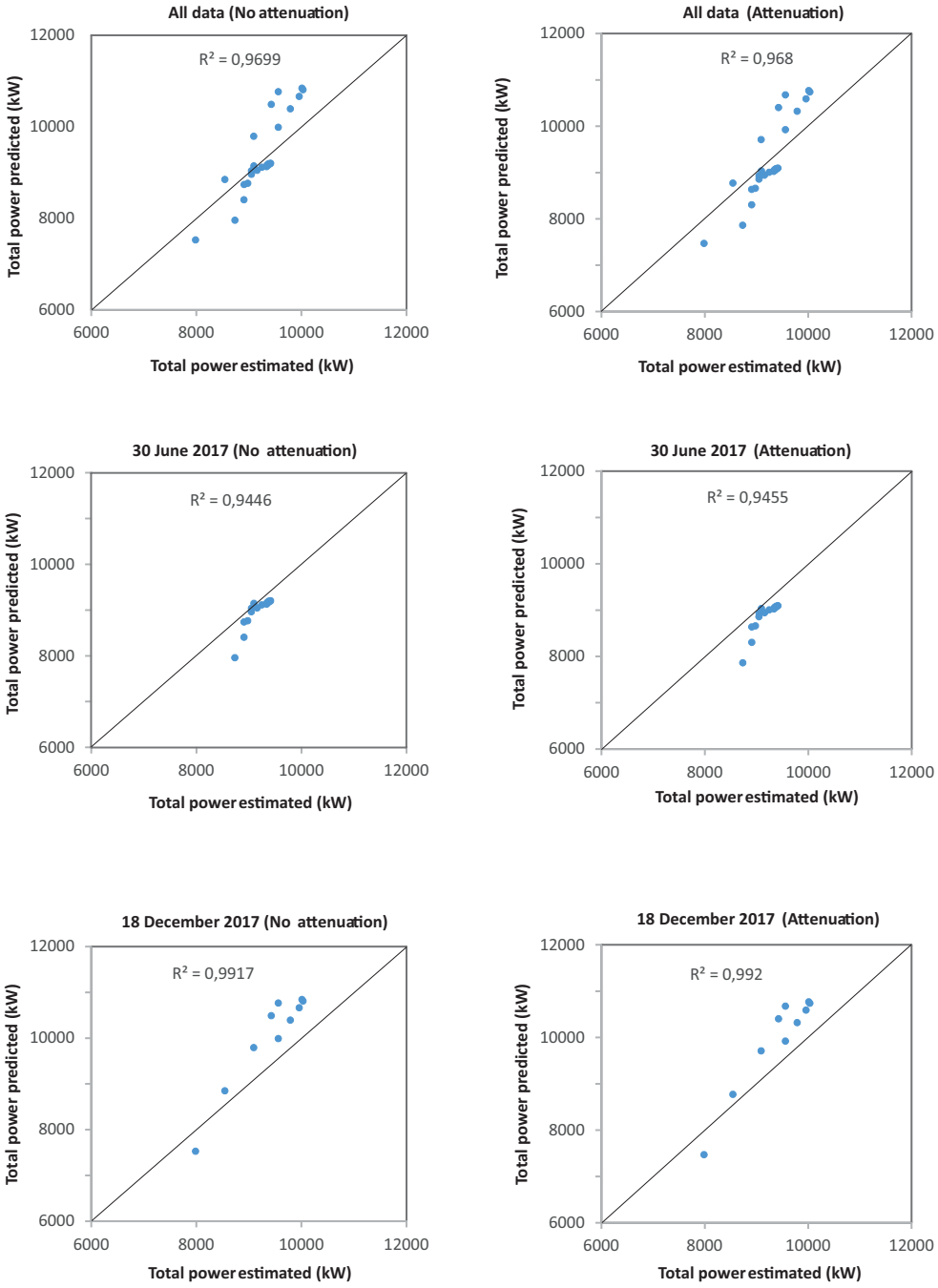

Figure 9: Correlation coefficient (R) for the predictions of P_E on target.

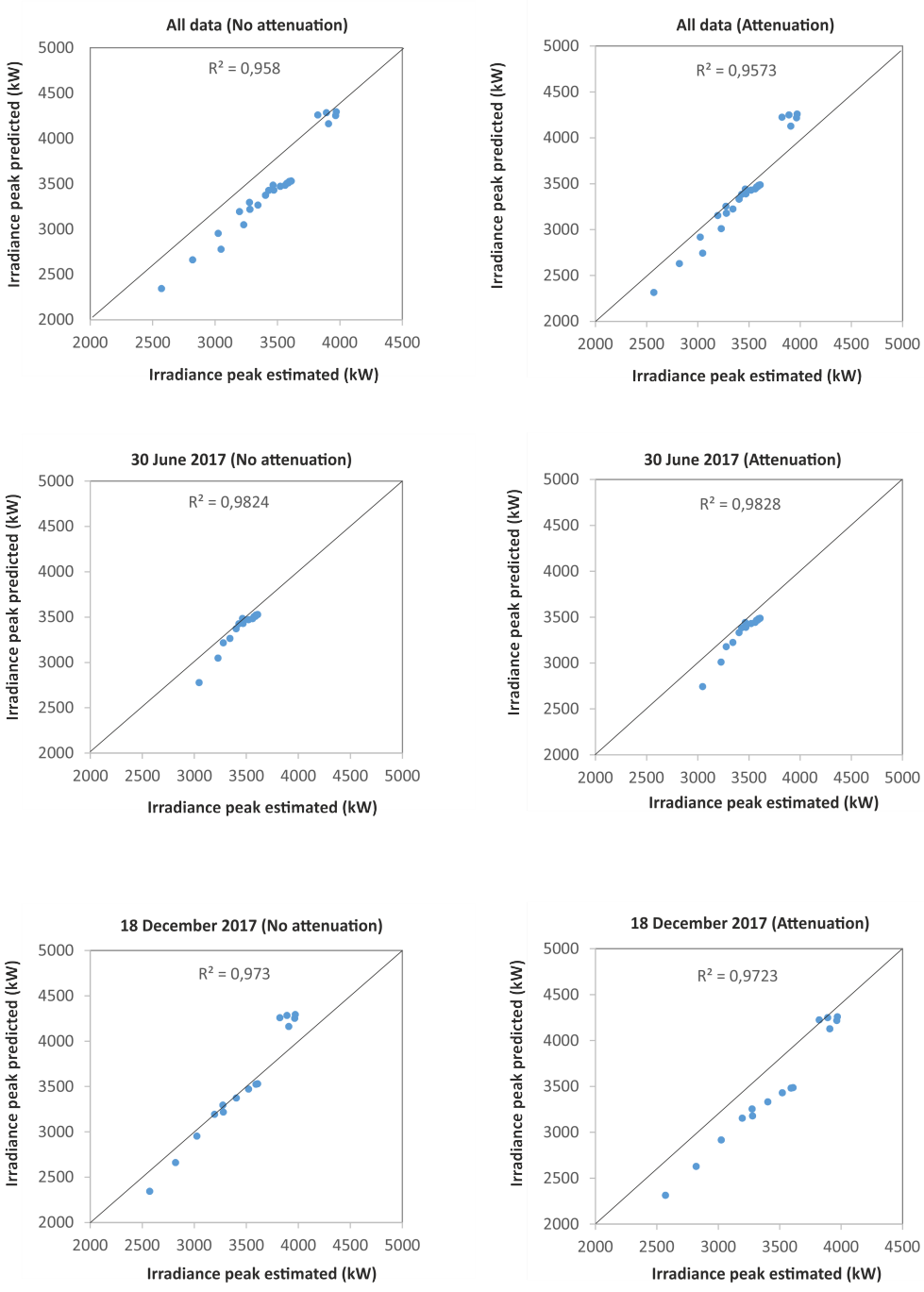

Figure 10: Correlation coefficient (R) for the predictions of E_{peak}.